Enhanced Cu(II) adsorption using sodium trimetaphosphate modified cellulose beads: equilibrium, kinetics, adsorption mechanisms and reusability

Najeh Maaloul[1], Paula Oulego[2] (http://orcid.org/0000-0002-3829-8960), Manuel Rendueles[2], Achraf Ghorbal[1,3](https://orcid.org/0000-0001-7340-3095), Mario Díaz[2*]

[1]Applied Thermodynamic Research Laboratory LR18ES33, National Engineering School of Gabes, University of Gabes, Avenue Omar Ibn El Khattab 6029 Gabes, Tunisia.

[2] Department of Chemical and Environmental Engineering, University of Oviedo, C/ Julián Clavería s/n, E-33071 Oviedo, Spain.

[3] Higher Institute of Applied Sciences and Technology of Gabes, University of Gabes, Avenue Omar Ibn El Khattab 6029 Gabes, Tunisia.

*Corresponding author's e-mail: mariodiaz@uniovi.es

Abstract

The current study is focused on the simple synthesis of two novel biosorbent beads: BASB/STMP and CNFB/STMP, derived respectively from bleached almond shell (BAS) and cellulose nanofiber from almond shell (CNF) by means of chemical crosslinking with sodium trimetaphosphate (STMP). These biosorbents were thoroughly characterized in terms of structure (FTIR), texture (N_2 adsorption-desorption), thermal behavior (TGA/DTG), morphology (SEM) and surface properties (XPS). The adsorption kinetics of Cu(II) ions onto BASB/STMP and CNFB/STMP materials proved the chemisorption interaction between Cu(II) ions and the STMP-functionalized beads. The BASB/STMP equilibrium data were successfully described by the Redlich-Peterson model and the CNFB/STMP data by the Sips model which disclosed maximum adsorption capacities of 141.44 mg g^{-1} and 147.90 mg g^{-1}, respectively. Furthermore, the BASB/STMP bioadsorbent offers easy regeneration and better reusability with high efficiency (> 83%). This study sheds light on the preparation of low-cost adsorbents for wastewater treatment

in order to improve the competitiveness and eco-friendliness of agrowaste-based processes.

Keywords: adsorption, almond shell, biosorbent beads, cellulose, crosslinking, Cu(II) ions, STMP-functionalized.

Introduction

The growing urbanization and industrial development result in the release into the environment of large amounts of industrial effluents containing high concentrations of toxic pollutants, such as Cu(II) ions (Dhandole et al. 2020), which can seriously threaten the ecosystems and human health (Bilgin and Erol 2018; Mikoda 2018; Qi et al. 2019). Therefore, effective treatment of wastewaters containing this heavy metal is among the most crucial problems. Several technologies have been evaluated to remove copper from contaminated water, including, chemical and biological treatments, ion exchange, membrane separation, and adsorption (El Rouby et al. 2018). It is necessary to analyze new technologies and novel-structured materials to remove soluble heavy metals from water streams. Within these technologies, adsorption is being widely studied to remove contaminants from wastewaters due to its flexibility and simplicity (Ben Arfi et al. 2017; Yang and Fox 2018). Moreover, the use of adsorbents from waste materials is essential to develop low-cost strategies for water treatment. In this sense, cellulose is an inexpensive and eco-friendly material, which has drawn much attention owing to its advantageous properties, such as its wide applicability in a variety of fields, the most remarkable ones being technological, medical, food applications and more recently wastewater treatment (Yang et al. 2020). In fact, there is an increasing interest in adding value to cellulose, which can be used for the synthesis of biosorbents for toxic heavy metal removal thanks to its ion exchange capacity and both chemical and mechanical stability (Reid et al. 2017). Besides, it can be easily functionalized to a variety of derivatives due to the presence in its structure of hydroxyl (–OH) and carboxyl (–COOH) groups (Ram and Chauhan 2018). Various forms and morphologies of cellulose-based adsorbents have been prepared for copper (II) ion uptake, such as powder (Maaloul et al. 2017a; Ahmad et al. 2018), nanofibers (Maaloul et al. 2017a), nanomaterials (Abou-Zeid et al. 2018), membranes (Awang et al. 2019) and beads (El Rouby et al. 2018; Ahmadpoor et al. 2019; Maaloul et al. 2019). Nevertheless, the preparation and chemical functionalization of adsorbent cellulose beads from agricultural wastes, such as almond

shell, is a topic of increasing interest due to the low price and great abundance of this waste (Maniscalco et al. 2020).

Sodium trimetaphosphate (STMP), a non-toxic reagent, has been commonly used as a crosslinking agent in the food industry (Sánchez-Reséndiz et al. 2018; Hu et al. 2019; Xie et al. 2019) as well as in the biomedical field (Leone et al. 2020). Specifically, it was successfully employed to enhance the adsorption capacity of wheat and corn starches, obtaining nontoxic functionalized adsorbents with remarkable resistance (Xie et al. 2019). For this reason, we have selected STMP as a crosslinker for polysaccharides. To the best of our knowledge, STMP-modified cellulose beads from agricultural waste have not been studied for the purpose of heavy metal removal.

Therefore, the aim of the present study was to develop a novel methodology for the preparation and STMP functionalization of bleached almond shell beads (BASB) and cellulose nanofibers from almond shell beads (CNFB) for copper (II) ion removal from aqueous solutions. The prepared beads were characterized using Fourier transform infrared spectroscopy (FTIR), scanning electron microscopy (SEM), X-ray photoelectron spectroscopy (XPS), nitrogen adsorption–desorption and thermo-gravimetric analysis (TGA). The influence of pH, the kinetics and isotherm models were fully investigated, and XPS measurements were used to elucidate the underlying adsorption mechanism. The reusability of adsorbents was explored by means of four adsorption-desorption cycles using HCl (0.1 M) as eluent. The multifunctional properties and the excellent adsorption performance of the prepared biosorbents indicated their potential applicability in actual wastewater treatment.

Materials and methods

Materials and reagents

Trisodium trimetaphosphate (STMP) (≥ 99.8 %), sodium hydroxide (NaOH) (≥ 98.8 %), hydrochloric acid (HCl) (≥ 37 %), 1-butyl-3-methylimidazolium chloride (BmimCl) (98 %), absolute ethanol (CH_3COOH) (≥ 99.9 %) and silicon oil were purchased from Sigma-Aldrich. Bleached almond shell (BAS) and TEMPO oxidized cellulose from almond shell (CNFs) were prepared according to the method described in our previous study (Maaloul et al. 2017b). Copper nitrate ($CuNO_3.\ 3H_2O$) (99 %) was purchased from Riedel de Haën. These chemicals were used without additional

purification unless otherwise stated. Distilled water was used for the preparation of all chemical solutions.

Preparation and modification of the adsorbents

The synthesis of STMP functionalized cellulose beads was performed through a two-step process: the first step was the preparation of cellulose beads from almond shell (BASB and CNFB) and the second one was the chemical modification of synthesized beads. BASB and CNFB were synthesized in the same way as in our previous study (Maaloul et al. 2019). Briefly, cellulose/BmimCl solution was prepared by dissolving 4 g of BAS and CNFs in powder form in 100 g of melted BmimCl and stirring at 120 °C for 2 h and 1.5 h, respectively. This cellulose/BmimCl solution was added dropwise into distilled water under constant stirring at 25 °C. The immediately formed hydrogel beads were washed several times with distilled water until the solution reached pH around 7. These synthesized hydrogel beads were frozen at -70 °C for 24 h. Then, the frozen beads were immersed in absolute ethanol for about 4 h and left to dry at 30 °C in an oven. The beads produced from BAS and CNFs are hereafter known as BASB and CNFB, respectively.

For the STMP modification of the beads, approximately 0.1 g of each bead type was placed in 200 mL of NaOH solution (5 wt%) and STMP. The mole ratio of the STMP/cellulose beads was 40. The mixture was shaken for 2 h at 30 °C. Afterwards, the beads were separated from the mixture and washed several times with distilled water to remove the remaining ions. Then, the modified cellulose beads were also washed with absolute ethanol. After the cleaning process, the resulting beads were dried in an oven at a temperature of 30 °C to obtain the BASB/STMP and CNFB/STMP adsorbents. The final product was packaged in containers for adsorption experiments.

Characterization techniques

The FTIR analyses were performed on a Two PerkinElmer spectrometer in attenuated total reflection (ATR) mode. The spectra were collected in the range of 600 to 4000 cm^{-1} (resolution: 2 cm^{-1}; 16 scans per sample). SEM images were recorded with a JEOL JMS-6610LV SEM instrument. Prior to the analysis, the samples were sputtered with gold to make them electrically conductive. The Brunauer-Emmett-Teller (BET) surface areas of the adsorbents were recorded by nitrogen (N_2) physisorption at -196 °C using a Micromeritics ASAP-2020. Thermogravimetric analyses (TGA/DTG) were

performed on a Mettler Toledo TGA/STDA851 instrument at a heating rate of 20 °C min^{-1} up to 900 °C under inert atmosphere (flow rate of N_2= 50 mL min^{-1}). About 6 mg of each sample were analyzed. XPS measurements were used to analyze the surface chemical states of the modified cellulose beads before and after metal ion adsorption. SPECS spectrometer equipped with a Phoibos 100 MCD analyzer and a monochromatized X-ray Al Kα (1486.6 eV) were used and the peak fitting was performed by Casa XPS software.

Swelling test of cellulose beads

The swelling behavior of the prepared materials was determined according to Wang et al. (2018c) from the mass change of dried beads after the immersion in water at room temperature for 24 h. The swollen beads were taken from the solution, and placed on a tissue paper to remove the unabsorbed water on the surface. The degree of swelling was measured according to equation (1)

$$Swelling\ \deg ree\ (SD\%) = \frac{W_S - W_d}{W_d} \times 100 \quad (1)$$

Where W_S is the weight of the swollen beads (g) and W_d is the weight of the dry beads (g).

Point of zero charge measurement

The pH_{PZC} of the adsorbents was measured by the following method: 0.1 g of dried biomaterial was put in glass flasks containing NaCl (0.05 M) solution. The initial pH of these solutions (pH_i) was adjusted to a series of values in the range of 1-9.5. After shaking for 48 h, the solutions were filtered and the final pH (pH_f) was recorded. The intersection point of the curve ΔpH (pH_i-pH_f) versus pH_i was taken as the pH_{PZC}.

Batch adsorption studies

The adsorption tests of Cu(II) onto cellulose beads (BASB/STMP or CNFB/STMP) were conducted in glass beakers (250 mL), containing 0.05 g of adsorbent and 100 mL of metal ion solutions. The suspension obtained was shaken in a temperature controlled orbital shaker at 30ºC and a constant rate of 90 rpm. The effect of solution pH, contact time and copper (II) initial concentration on the bioadsorption process was thoroughly investigated. The initial pH of Cu(II) solution was adjusted to the desired values, using

HCl and/or NaOH solutions. The concentration of Cu(II) in the solution was analyzed by ICP-MS. The sorption capacity at time t, q_t (mg g^{-1}) was calculated from equation (2)

$$q_t = \frac{(C_0 - C_t)V}{W_d} \quad (2)$$

where C_0 is the initial metal concentration (mg L^{-1}), C_t is the metal concentration at time t (min), V is the solution volume (L) and W_d is the mass of biosorbent (g).

Effect of pH variation on Cu(II) adsorption

The effect of the initial solution pH on copper adsorption was conducted over a pH range of 2.0–6.0. A given amount of adsorbents was added to the prepared Cu(II) solution with different pH and then shaken at a constant temperature of 30 °C and 90 rpm for 6 h. The adsorption capacity of Cu(II) ions, q_e (mg g^{-1}) was calculated using equation (3)

$$q_e = \frac{(C_0 - C_e)V}{W_d} \quad (3)$$

where, C_0 is the initial metal concentration (mg L^{-1}), C_e is the metal concentration at equilibrium (mg L^{-1}), V is the solution volume (L) and W_d is the adsorbent mass (g).

Adsorption kinetics and isotherm

The adsorption kinetics and isotherms were obtained under the conditions described above. In short, the adsorption kinetics were evaluated in a 200 mg L^{-1} Cu(II) solution of pH 6. The adsorption isotherms were obtained by shaking Cu(II) ion solutions (pH 6) with different initial concentrations ranging from 25-600 mg L^{-1} for BASB/STMP and from 25-1000 mg L^{-1} for CNFB/STMP. The adsorption capacities (q_e, mg g^{-1}) were also calculated according to equation (3).

The experimental data were fitted by non-linear regression analysis using OriginPro v8.0 software. The determination coefficient (R^2) and reduced chi-square (χ^2) were used to evaluate the best fit between kinetic or isotherm models and experimental data. The applicability of a model is witnessed by higher R^2 values and lower χ^2 values.

Regeneration of BASB/STMP and CNFB/STMP

The regeneration properties of BASB/STMP and CNFB/STMP were tested with an acidic solution (HCl, 0.1 M). After agitating 0.05 g of the adsorbents (BASB/STMP or CNFB/STMP) with 100 mL of Cu(II) ions (200 mg L^{-1}) at 30 °C for 2 h, the metal-loaded

adsorbents were collected by means of a 0.45 μm membrane filter, while the concentration of metal ions in the filtrate were determined by ICP-MS spectroscopy. Then the residue was rinsed with distilled water and desorbed with (0.1 M) HCl for 2 h. After that, the adsorbent was separated by filtration, and used for the next adsorption experiment. The cycle above was repeated four times. The regeneration rate of beads for the n^{th} regeneration (RR_n) was calculated by equation (4).

$$RR_n(\%) = \frac{q_n}{q_0} \times 100 \quad (4)$$

Where q_0 is the adsorption capacity of new beads (mg g^{-1}), q_n is the adsorption capacity of beads after the n^{th} regeneration cycle (mg g^{-1}).

Results and discussion

Characterization studies

FTIR spectra analysis

The FTIR spectra of the cellulose beads before and after modification with STMP reagent are depicted in Fig. 1(a-b). All the spectra of the prepared materials showed a band in the 3324-3359 cm^{-1} range corresponding to the stretching vibration of the hydroxyl group in cellulose molecules (Othmani et al. 2017; Milani et al. 2018). After the STMP modification of BASB and CNFB, the OH bands were shifted to lower wavenumbers due to the weakening of hydrogen-bonding interaction as a result of the functionalization of oxygen atoms of cellulose with phosphate ester groups (Wang et al. 2017). The peak observed in the range 2890-2894 cm^{-1} are due to CH_2 asymmetric stretching vibration (Milani et al. 2018). The peak at ~1641 cm^{-1} in all the spectra corresponds to the bending vibration of hydroxyl group of water absorbed in the cellulose beads structure (Liu et al. 2019). The peak present at 1605 cm^{-1} for the CNFB material is attributed to carboxylate groups (Maaloul et al. 2017a). Another broad band at 1305 cm^{-1} was associated with the CH_2 group in the samples without STMP reagent (Hemmati et al. 2018). Cellulose characteristic peaks were distinguished at 1159 cm^{-1} (C–O–C glycoside bond asymmetrical stretching), at 1017 cm^{-1} (C–O–C pyranose ring vibration) and 895 cm^{-1} (β-glycosidic bond bending) corresponded to the cellulose characteristics (Hemmati et al. 2018). These peaks are more intense in the BASB/STMP and CNFB/STMP samples. In order to verify the changes in the cellulose bead structures due to chemical modification, the major FTIR region of phosphate esters (1500-1140 cm^{-1})

was carefully analyzed (see Fig. 1b). The results show an increase in the peak intensity in the phosphate ester region for both the phosphorylated BASB and CNFB (at around 1156 cm^{-1}) (Sánchez-Reséndiz et al. 2018). Besides, characteristics peaks of the stretching (at 1368 cm^{-1}) and bending (at 1236 cm^{-1} for BASB/STMP and 1314 cm^{-1} for CNFB/STMP) vibrations of P=O group were also observed, thus confirming the successful functionalization of the adsorbents with phosphate ester group (Souto-maior and Reis 2010). It was also obtained a band at 1418 cm^{-1}, which is related to the formation of P–O–C bonds between the polysaccharide and the STMP (Souto-maior and Reis 2010). For the CNFB/STMP sample, the peak at 1278 cm^{-1} corresponded to the O=P–O double bond from the cyclic trimetaphosphate (Leone et al. 2020) and that at 996 cm^{-1} to P–O bonds (Hu et al. 2019; Leone et al. 2020). However, these two peaks are not present in the FTIR spectra of the BASB/STMP, which indicates that the STMP has reacted with the OH groups of the CNFB, leading to the formation of covalent linkages (Tao et al. 2016). This was later further verified by XPS analysis. Another high intensity peak beyond 1200 cm^{-1} (characteristic region of compounds with a large number of phosphate ester groups) was observed on BASB/STMP and CNFB/STMP sorbents. Similar FTIR results were reported by other authors when pectin (Souto-maior and Reis 2010), and soybean and peanut proteins (Sánchez-Reséndiz et al. 2018) were modified with STMP.

The band around 1480-1430 cm^{-1} is employed to determine the overall degree of order and crystallinity bands of cellulosic materials (Bregado et al. 2019), while the band at 893-897 cm^{-1} is associated with the amorphous region in cellulose (Li et al. 2019a). The absorption ratios of bands (1429 cm^{-1}/897 cm^{-1}) are defined as LOI (Lateral Order Index), which was proposed in the literature by Khan et al. (2019) and Bregado et al. (2019) to estimate the degree of crystallinity of cellulose. In this sense, high values of LOI corresponds to an elevated crystallinity index of cellulose and highly ordered cellulose chains (Khan et al. 2019). The LOI value can be determined as follow (equation 5)

$$LOI = \frac{A_{1429\ cm^{-1}}}{A_{897\ cm^{-1}}} \quad (5)$$

Where $A_{1429\ cm\text{-}1}$ and $A_{897\ cm\text{-}1}$ are the absorbancies at 1429 cm^{-1} and 897 cm^{-1}, respectively.

The calculated LOI values of the BASB, BASB/STMP, CNFB and CNFB/STMP samples were 0.41, 0.78, 0.45 and 2.38, respectively. Therefore, it can be concluded that the absorbance ratios of cellulose beads increased after the STMP cross-linking modification. These results indicated that the short-range molecular order of bead samples was disrupted by the crosslinking reaction. Hence, it was revealed that CNFB/STMP cellulose chains were much more ordered compared with BASB, BASB/STMP and CNFB.

XPS analysis

X-ray photoelectron spectroscopy (XPS) was utilized to further ascertain the material composition and verify the suitable crosslinking of STMP on the bead surface. The overall and high resolution XPS spectra of biosorbents are shown in Fig. 2(a-d). In the wide-scan spectra, the characteristic signals of C1s (285 eV), O1s (532 eV) and P2p (133 eV) were all detected. The functional groups of the modified cellulose beads were further revealed by C1s spectra (Fig. 2b). BASB/STMP and CNFB/STMP samples showed three characteristic functional groups of cellulose with binding energy at 282.46, 284.25 and 286.05 eV corresponding to C1 (C–C/C–H), C2 (C–OH/C–O–C), and C3 (C–O–C/C=O), respectively (Zhuang et al. 2019). Apart from the three common peaks with cellulose (Chen and Liu 2019), a new low intensity signal, named as C4, was identified in the CNFB/STMP material, which can be assigned to the O–C=O linkages of ester.

The high-resolution spectrum of O1s region (Fig. 2c), shows three signals with binding energies around 529.83, 531.60 and 532.69 eV. The peak at 529.83 eV was assigned to the carbonyl (C=O or O−C=O) groups, the peak at 531.60 eV to hydroxyl or ether groups and the peak at 532.69 eV may correspond to the R−O−R group (Oh et al. 2019). Hu et al. (2019) reported that the O1s spectrum around binding energies 529.83 and 532 eV might be attributed to the O–P bond formed between cellulose and STMP and to non-bridging (P−O) oxygen (Rol et al. 2020).

As shown in Fig. 2d, the peak at 133 eV is P2p (Xie et al. 2019) confirms the successful inclusion of phosphate in the BASB and CNFB materials. The high resolution XPS spectra of P2p in Fig. 2d showed two binding energies at 131.17 and 133.6 eV for BASB/STMP and 131.17 and 134.3 eV for CNFB/STMP, which could be due to phosphate molecules bound to carbon (P−C) and oxygen atoms (P−O) and/or oxidized phosphate (P=O). These results are in good accordance with the FTIR analysis.

Morphological properties of biosorbents

The surface morphology and internal structure of the biosorbents are shown in Fig. 3(a-h). Clearly, Figs. 3(a) and 3(e) show that the shape of the beads was mainly spherical with irregular surface, the average diameter being around 3 mm. Furthermore, the BASB/STMP material exhibited a more porous surface structure and a rougher surface than the CNFB/STMP one. Based on Fig. 3e, it can be seen that the morphology of the CNFB/STMP is almost nonporous, irregular and shriveled. It can also be noticed from the high magnification images (Fig. 3b and f) that the surfaces of BASB/STMP and CNFB/STMP are wrinkled after introducing STMP into BASB and CNFB. A more detailed structural characterization of the representative beads is presented in (Fig. 3c, d, g, h). The SEM images (Fig. 3c and g) revealed that BASB/STMP and CNFB/STMP materials can potentially act as porous matrix supports. The fine surface structure (Fig. 3d and h) showed that their cross-sections were fixed by STMP and there were interconnected, irregular pores and cavities in the interior of the spherical particle. Hence, the STMP introduced into cellulose beads by NaOH aqueous solution could result in a larger specific surface compared to the unfunctionalized beads. The porous structure of the cellulosic beads may improve the diffusion of metal ions into the internal pores of bioadsorbent through the porous channels (Putra and Lee 2019).

Specific surface area analysis

The textural properties of the adsorbents before and after the functionalization was accomplished by N_2 adsorption-desorption isotherms. As depicted in Fig. S1, it can be observed that all the isotherm curves presented a hysteresis loop, indicating the existence of macro-mesopores (Olivera et al. 2018). The BET specific surface areas (S_{BET}) were calculated to be 0.007, 0.87, 0.57, 1.22 m^2 g^{-1} for BASB, BASB/STMP, CNFB and CNFB/STMP, respectively (Table 1). Compared to the unfunctionalized beads, the S_{BET} of BASB/STMP was increased 117 times, whereas the increase turned out to be much more moderate for CNFB/STMP compared to CNFB (2.15 times). The improvement in S_{BET} of both bio-beads could be attributed to the presence of STMP, which has a rougher surface texture. Despite the increase in the specific surface areas, the S_{BET} of CNFB/STMP was still much higher than that of the BASB/STMP sample.

The specific surface areas of almond shell powder, cellulose extracted from almond shell and other adsorbent beads were reported in Table 1. Obviously, by comparison with

other adsorbent beads referred to in the literature, the large value of BET surface area for the CNFB/STMP can be expected to be highly advantageous for the removal of heavy metal ions from contaminated water. Therefore, STMP reagent played a significant role in improving the textural properties of BASB and CNFB.

Thermal degradation of adsorbents

The thermal properties of STMP-functionalized and unfunctionalized beads was investigated using thermogravimetric analysis, and the resulting TGA and DTG thermograms are displayed in Fig. 4(a-b). The four samples showed three main thermal degradation patterns. The first weight reduction was observed over the temperature profile of 70 to 125 °C corresponding to the evaporation of moisture and weakly attached water (Oun and Rhim 2019). The weight losses at this stage were 7.3%, 10%, 4.8% and 9.4% for BASB, BASB/STMP, CNFB and CNFB/STMP, respectively. The main weight loss was observed in the 206-400 °C range due to the depolymerization of hemicellulose and cellulose units (Maaloul et al. 2019). The onset decomposition temperatures of hemicellulose (T_{onset}) for BASB/STMP and CNFB/STMP were 220 °C and 213 °C, respectively. The maximum heat degradation processes for the unmodified cellulose beads is observed at 286 °C (for BASB) and 270 °C (for CNFB). While cellulose decomposition occurs in the 311 to 408 °C range, the highest degradation rate appears at 343 °C for BASB and 336 °C for CNFB. The major weight-loss process of BASB/STMP and CNFB/STMP, as shown in Fig. 4a, was increased due to the improved thermostability of carbon layers when the oxygen groups of cellulose reacted with STMP. The mass loss (~ 40%) in the 210–500 °C range corresponded to the decomposition of both phosphate ester groups and the residual oxygen-containing functional groups (Wang et al. 2017). In fact, the shift in the onset degradation temperature towards higher values could be related to the depolymerization of cellulose chains that reacted with the phosphate ester groups, as discussed in the FTIR analysis. Similar changes in the thermal behavior was observed when wheat starch was treated with STMP (Xie et al. 2019).

The DTG patterns of BASB/STMP and CNFB/STMP were somewhat similar. The largest weight losses (T_{max}) corresponded to the DTG curves of both samples, which can be explained by the overlapping of cellulose and hemicellulose, resulting in a unique peak observed at 307 °C for BASB/STMP and 313 °C for CNFB/STMP (Fig. 4b). The final residues that remained at 900°C for BASB/STMP (21.17 %) and CNFB/STMP (10.08 %) were significantly higher than those of BASB (13.04 %) and CNFB (4.47 %). This can

be due to the introduction of inorganic minerals during the functionalization process. Basing on the fact that thermal stability of cellulose is closely related to its crystallinity, it can be stated that, the higher the LOI value, the greater the thermostability of tested samples (Ahmadzadeh et al. 2016). All of these observations indicate that the STMP crosslinked beads possess high heat resistance as compared to native cellulose beads. The improved thermal resistance of the adsorbents is a desirable feature for the remediation of pollutants from water (Ben Arfi et al. 2019).

Swelling study

The swelling behavior of the prepared bio-beads was studied for comparison purposes (Fig. S2). All the cellulose beads showed an excellent swelling degree (SD), since the minimum value was higher than 155 %. This is due to the fact that the prepared materials have more hydrophilic groups which can absorb large amounts of water molecules, while exhibiting a three-dimensional network structure, which facilitates free water entrainment (Luo et al. 2018a). As shown in Fig. S2, the water-swelling capacity of BASB decreased from 207.5 % to 155 % after the STMP functionalization because the crosslinking of BASB by STMP caused the pores of the resulting structure to shrink (Ma et al. 2016). The crosslinking of phosphate groups may have decreased the number of water-holding groups in the structure. Ma et al. (2016) reported a similar swelling tendency for STMP modified porous spheres in water. Fig. S2 revealed that the SD of CNFB/STMP increased after the incorporation of STMP. The significant increase in the swelling capacity of the CNFB/STMP is most likely related to the polymeric network cohesion and cavity (SEM analysis (Fig. 3)) (Luo et al. 2019).

The analysis results of the FTIR, and XPS analysis and the pH_{pzc} values of both studied beads showed abundancy of the carboxyl, hydroxyl and phosphate ester groups on the modified BASB and CNFB. The existence of such groups may play a critical role in the biosorption of Cu(II). The details of the adsorption mechanisms will be investigated in the section below.

Batch adsorption experiments

Influence of pH on metal ions removal

The effect of pH on Cu(II) adsorption over the BASB/STMP and CNFB/STMP samples were studied at various initial pH values between 2 and 6 (Fig. 5), disclosing that there is a significant increase in the degree of Cu(II) adsorption at pH 2−6. The poor metal

removal at highly acidic pH 2−3 is due to the protonation of hydroxyl, carboxylic and phosphate groups, which causes repulsion of the metal ions. Subsequent increases (pH 4−6), led to improved adsorption capacity due to the decreased H^+ ion concentration (Ahmad et al. 2018; Ahmadifar and Koohi 2018; Wang et al. 2018d). The adsorption of copper on the surface of the particles may be favorable at pH> pH_{pzc}, which was found to 7.25 for BASB/STMP and 7.1 for CNFB/STMP (Fig. S3). As a result, when the pH of an adsorbate solution is higher than the corresponding pH_{pzc}, the surface charge of the bioadsorbent is negative, whereas the opposite is true when the pH of the adsorbate solution is lower than pH_{pzc} (Lawal et al. 2019). The $CuNO_3$ solution caused metal hydroxide precipitation when the pH was higher than 6, thereby making the metal adsorption studies impossible (Wang et al. 2018a). Therefore, a pH value of 6 was selected as the optimal one for Cu(II) ion adsorption on both adsorbents. Similar results were achieved in previous studies (Maaloul et al. 2017a; Ahmad et al. 2018; Wang et al. 2018a; Wang et al. 2018d).

Adsorption kinetics

To evaluate the effect of contact time on Cu(II) adsorption onto functionalized beads, kinetic studies were carried out at a fixed concentration of 200 mg L^{-1}, pH 6 and at 30 °C (Fig. 6(a-b)). Fig. 6a presents the adsorption capacity of metal ions over BASB/STMP and CNFB/STMP at different time intervals. Fig. 6a clearly shows that the uptake rate of copper increased by increasing the reaction time and reached an equilibrium state. The kinetic data revealed a fast adsorption rate within the initial 120 min for BASB/STMP and 60 min for CNFB/STMP. It is a reasonable to attribute this phenomenon to the availability of free actives sites on the beads surface (Qi et al. 2018).

To describe the sorption kinetics behavior of the beads, three different models have been used, which rely on pseudo-first-order, pseudo-second-order and intraparticle diffusion mechanisms, as depicted in Fig. 6(a-b). The pseudo-first-order and pseudo-second-order models can be expressed by equations (5) and (6), respectively:

$$q_t = q_e\left(1 - e^{-k_1 t}\right) \tag{5}$$

$$q_t = \frac{q_e^2 k_2 t}{1 + q_e k_2 t} \tag{6}$$

where q_e (mg g^{-1}) and q_t (mg g^{-1}) are the adsorption capacities of the adsorbents at equilibrium and time "t" (min); k_1 (min^{-1}) and k_2 (g mg^{-1} min^{-1}) are the rate constants for the corresponding model in the equations (5-6). The calculated parameters of the pseudo-first-order and pseudo-second-order models are compiled in Table 2.

By comparison of the correlation coefficients (R^2) of BASB/STMP and CNFB/STMP samples, the pseudo-second -order kinetic model proved to be the most suitable one for the description of the copper removal process, where the R^2 values exceeded 0.99 (Table 2). In addition, the theoretical (q_e) value and experimental results are in good agreement with each other. It is concluded that the pseudo-second-order model is more appropriate to explain the adsorption mechanism for STMP functionalized beads. The obtained results implied that the biosorption process was controlled by the chemical reactions (Wang et al. 2018d; Maaloul et al. 2019; Wen et al. 2020).

Intraparticle diffusion mechanism of adsorption

The diffusion mechanism cannot be explained using the pseudo-second order kinetic model. Thus, it was evaluated by the theory proposed by Weber and Morris (1963), which relies on an internal model commonly used to describe the diffusion of the adsorbate into the adsorbent, as is expressed by equation (7). The experimental data were fitted to the Weber and Morris model to verify if the internal diffusion step is controlling the whole adsorption process (Wen et al. 2020). The fitting results are shown in Fig. 6b and the calculated internal diffusion rate constant and R^2 values are given in Table 2.

$$q_t = k_{WB} t^{1/2} + I \quad (7)$$

where, k_{WB} is defined as the Weber and Morris rate constant (mg g^{-1} $min^{-0.5}$), and I is the thickness of the boundary layer (mg g^{-1}). The slope and intercept of linear plots of q_t against $t^{1/2}$ yield the values of k_{WB} and I.

The linearized graph in Fig. 6b and kinetic parameters in Table 2 showed that the BASB/STMP plots were divided into three steps based on the three sequential straight lines, while the CNFB/STMP graph was separated into two steps. The first stage in all the samples describes the liquid film diffusion (Singh et al. 2017). The fitting plotted in the first stage did not pass through the origin, indicating that diffusion into beads was not the only rate-limiting step (Chang et al. 2020). Afterwards, at the second stage, the copper

ions were transferred and adsorbed into the pores of the particles, resulting in an intraparticle diffusion rate-limiting step (Ballav et al. 2018). The data fitting in the third stage for the BASB/STMP sample was assumed to correspond to adsorption equilibrium (Chang et al. 2020). Further, as shown in Table 2, the values k_{id} for the second and the third stages were lower than those of the first stage, which was due to the slowing of intraparticle diffusion as the concentration of copper in the solution decreased (Singh et al. 2017; Chang et al. 2020). In summary, the adsorption mechanism of Cu(II) ions on BASB/STMP and CNFB/STMP were successfully explained by both the pseudo-second-order and intraparticle diffusion models.

Equilibrium adsorption isotherm

The adsorption isotherms are intended to disclose the relationship between the adsorbate and the adsorbent, knowing that the interaction between the surface and the adsorbate might occur through chemisorption or physisorption (Somsesta et al. 2020). Figure 7(a-b) displays the adsorption isotherm of Cu(II) ions on BASB/STMP and CNFB/STMP biosorbents. Five adsorption isotherms including, Langmuir, Freundlich, Redlich-Peterson, Sips and Dubinin-Radushkevich models were applied to fit the experimental date and explain the equilibrium adsorption. The details related to each of the models can be found in section 4 of the Supplementary Material.

Fig. 7a and b are plots of the nonlinearized Langmuir, Freundlich, Redlich-Peterson, Sips and Dubinin-Radushkevich isotherms. The calculated values from the five isothermal adsorption parameters along with their determination coefficient (R^2) and reduced Chi-square (χ^2) are presented in Table 3. The highest estimated R^2 and the smallest (χ^2) values are regarded as measurements of the goodness of fit to the experimental data. The applicability of the five isotherm models to the present data follows the approximate order:

BASB/STMP: Redlich-Peterson> Dubinin−Radushkevich> Langmuir> Sips > Freundlich.

CNFB/STMP: Sips> Langmuir> Dubinin−Radushkevich> Redlich-Peterson> Freundlich.

According to the R^2 and χ^2 values, Redlich-Peterson model is the most suitable to describe the experimental data for BASB/STMP while Sips model is the most accurate for CNFB/STMP. Redlich-Peterson model offers a compromise between Langmuir and

462 Freundlich models by assuming that the mechanism of adsorption is a hybrid one, which
463 deviates from ideal monolayer adsorption (Syafiuddin et al. 2018). Sips model is a
464 combination of both Langmuir and Freundlich isotherm models. This model permits to
465 predict the heterogeneity of adsorption systems (Neris et al. 2018). It was conceived in
466 an attempt to avoid the limitation of the sorbate concentration associated with the
467 Freundlich isotherm (Stanciu and Nichifor 2018). The maximum adsorption capacities of
468 Cu(II) ions achieved by BASB/STMP and CNFB/STMP were 141.44 mg g^{-1} and 147.90
469 mg g^{-1}, respectively.

470 The mean free energy (E) of sorption per molecule of sorbate was calculated to
471 predict the type of adsorption mechanism, the values being 12.91 kJ mol^{-1} and 9.13 kJ
472 mol^{-1} BASB/STMP and CNFB/STMP, respectively. Since the values are higher than 8 kJ
473 mol^{-1}, chemisorption was involved in the adsorption process of BASB/STMP and
474 CNFB/STMP. Similar trends were reported by other researchers (Lei et al. 2018; Maaloul
475 et al. 2019).

476 **Comparison of the adsorption capacity**

477 The maximum Cu(II) adsorption capacities of BASB/STMP and CNFB/STMP
478 found in this work were 141.44 mg g^{-1} and 147.90 mg g^{-1}, respectively. This result was
479 compared with various adsorbents prepared by other authors, as listed in Table 4.
480 Comparatively, the CNFB/STMP showed higher adsorption capacity when compared to
481 the bleached almond shell powder, porous cellulose sphere, TEMPO oxidized cellulose
482 nanofibers and cellulose beads from bleached almond shell. The big advantage of
483 BASB/STMP and CNFB/STMP over those powdered adsorbents was the ease of
484 recovery and separation from effluents after treatment. Hence, the STMP functionalized
485 cellulose beads can be seen as promising adsorbents for copper (II) removal from polluted
486 water; this is especially true for CNFB/STMP, as it possesses the highest adsorption
487 capacity value.

488 **Reusability**

489 Reusability of BASB/STMP and CNFB/STMP for Cu(II) adsorption/desorption
490 was performed in four consecutive cycles and the results of the analysis are presented in
491 Fig. 8. As can be seen, the adsorption properties of BASB/STMP remain unchanged for
492 all cycles. Only a slight decrease in the mean adsorption value can be observed for copper
493 (83%), thereby indicating that the prepared BASB/STMP could be a promising candidate

for highly toxic ion removal, such as copper (II). On the other hand, the regeneration rate of Cu(II) ions by CNFB/STMP material dropped to 55% of its initial adsorption capacity. This difference reflects the higher affinity for Copper (II) ions of CNFB/STMP than BASB/STMP, which might be attributed to the stronger bonding ability between metal ions and the hydroxyl, carboxylic and phosphate-groups on the CNFB/STMP surface. That is to say, a higher proportion of active sites on CNFB/STMP occupied by Cu(II) ions could not be completely desorbed by HCl under the same conditions. Overall, the data obtained in the reusability experiment showed that the regeneration of BASB/STMP in HCl (0.1 M) solution is a suitable, simple and cost-effective process that does not damage the structure of the sorbent.

Mechanism of interactions between the adsorbate and adsorbent

The above-mentioned results showed the excellent adsorption performance of the BASB/STMP and CNFB/STMP for Cu(II) ion removal. This is can be explained considering the abundance of functional groups on the adsorbent surface (Wang et al. 2018b). in order to analyse in depth the adsorption mechanism of STMP functionalized beads, XPS analysis was used to gain better understanding of the interaction between the hydroxyl, carboxylate and phosphate ester groups with Cu(II) ions. As expected, in Fig. 9a, a small Cu 2p peak appeared in the XPS survey spectra of BASB/STMP-Cu and CNFB/STMP-Cu at around 934 eV. The high resolution of Cu 2p the spectrum (Fig. 9b) can be deconvoluted into two peaks located at 931.45 eV (assigned to Cu $2p_{3/2}$) and 952.13 eV (assigned to Cu $2p_{1/2}$) (Zhang et al. 2019; Dhandole et al. 2020). The peak of Cu $2p_{3/2}$ could be attributed to the reaction between Cu(II) and oxygenated groups bounded to the surface of the cellulose beads, and the peak of Cu $2p_{1/2}$ probably formed by the reaction of OH groups (Dhandole et al. 2020).

Fig. 9c shows the C1s spectrum after adsorption, in which five representative signals at ~283 eV, 284–285 eV, ~286 eV, ~287 eV and ~288 eV were identified as –C–H, –C–(C, H)/C=C, –C–C, –C=O and O–C=O, respectively (Chen and Liu 2019; Zhuang et al. 2019) for both BASB/STMP-Cu and CNFB/STMP-Cu. The peak deconvolution results showed that the relative percentage of the (C–C/C–H) and (C–O–C/C=O) peaks shifted and decreased on the BASB/STMP-Cu and CNFB/STMP-Cu samples, meaning that these functional groups may be involved in the adsorption process.

In the O1s spectrum (Fig. 9d), the main peak was decomposed into another three peaks, which could be due to the binding energies of the C=O or O–C=O, O–H, C–O–C and P–O level at ~529 eV, ~530 eV, ~531 eV and ~532 eV, respectively (Dhandole et al. 2020; Rol et al. 2020). All the resolved O1s XPS spectrum demonstrated the shift of bending energy after adsorption, revealing that the corresponding active oxygen-containing groups also participated in the formation of the coordinated bonds (O → Cu(II)) (Godiya et al. 2019). The relative percentage of O1s spectra in CNFB/STMP-Cu sample decreased significantly, confirming that the carboxylic and hydroxyl groups in CNFB/STMP are involved in the Cu(II) adsorption, in which the O atom donates the lone pair of electrons to the metal ion and the resulting electron density around the O atom decreases (Ahmad et al. 2018). The significant difference between C1s and O1s peaks demonstrated that the oxygen-containing groups (such as hydroxyl and carboxyl groups) in the cellulose beads participated in strong complexing reactions with Cu(II) (Zhan et al. 2019; Zhang et al. 2020).

Nevertheless, the scan spectra of P2p of the BASB/STMP-Cu and CNFB/STMP-Cu samples were deconvoluted into four peaks as depicted in Fig. 9e. The binding energies at 131.85 eV, 132.29 eV, 133.80 eV and 134.75 eV for BASB/STMP-Cu can be associated with the dominant groups P–C, P–O, $(PO_4)^{3-}$ and $(PO_3)^{-}$, according to the references found in the existing literature (Orliukas et al. 2013; Zhou et al. 2018). This difference in binding energies stems from different bonds of phosphorus such as P–O, P–O–P (or double bond P=O), $O=P(OR)_3$ and P–O–C (or P–OH) (Li et al. 2019b). The P2p spectra of CNFB/STMP-Cu are almost identical to those of BASB/STMP-Cu. It can be concluded from Fig. 9e that both the intensity and area ratio of P2p decreased after Cu(II)-loaded at 131.85 eV and 133.8 eV for BASB/STMP-Cu and 131.53 eV and 134.45 eV for CNFB/STMP-Cu. Compared with those obtained prior to the adsorption, the location of P2p peaks shifted towards higher binding energies for all the sorbents. The highest core-level binding energies were related to formation of oxides with cations (Fongkaew et al. 2017). This finding confirms that C1s, O1s and P2p spectrum may be involved in the main chemisorption of metal ions, which was also reported in a recent study (Li et al. 2019b).

Conclusion

The biosorbents BASB/STMP and CNFB/STMP were prepared from almond shell to remove Cu(II) ions from aqueous solution and characterized by SEM, FTIR, XPS, BET

and TGA/DTG. Due to the modified hydroxyl and carboxyl groups on the surface of the material, BASB/STMP and CNFB/STMP showed good adsorption performance for Cu(II) ions, the corresponding adsorption capacities being 141.44 and 147.90 mg g^{-1}. These values were higher than those of various commercially available adsorbents, including activated carbon and modified biosorbents. Cu(II) adsorption kinetics were best fitted to a pseudo-second order kinetic model, showing equilibrium adsorption after 120 min for BASB/STMP and 60 min for CNFB/STMP. A series of isotherm models were put forward and the data obtained were successfully fitted to the Redlich-Peterson and Sips model for BASB/STMP and CNFB/STMP, respectively. The adsorption mechanisms, including surface complexation and ion exchange, were verified from the adsorption properties and the adsorbent characterization after adsorption by means of XPS measurements. The reversibility of the adsorption–desorption process in HCl (0.1 M) solution indicates that STMP-modified beads may be considered as efficient biosorbents for heavy metal ion removal from aqueous solution. The BASB/STMP sample showed excellent performance in terms of regeneration and reuse, the results being superior to those achieved by the CNFB/STMP bead. The potential applicability of the modified material offers great possibilities for the revalorization of agricultural wastes, thus making this industry more competitive and environmentally friendly.

Acknowledgement

Authors acknowledge the financial support from the Employment, Industry and Tourism Office of the Principality of Asturias (Spain) through the project GRUPIN IDI/2018/000127. Authors also thank the Scientific and Technical Services of the University of Oviedo for their technical assistance with sample analyses. We would like to thank Dr. J. Espina from the electronic and vibrational spectroscopy unit, for all his assistance with XPS analysis.

References

Abou-Zeid RE, Khiari R, El-Wakil N, Dufresne A (2018) Current State and New Trends in the Use of Cellulose Nanomaterials for Wastewater Treatment. Biomacromol. doi: 10.1021/acs.biomac.8b00839

Ahmad M, Manzoor K, Ahmad S, Ikram S (2018) Preparation, Kinetics, Thermodynamics, and Mechanism Evaluation of Thiosemicarbazide Modified Green Carboxymethyl Cellulose as an Efficient Cu(II) Adsorbent. J Chem Eng Data 63:1905–1916 . doi: 10.1021/acs.jced.7b01008

Ahmadifar Z, Koohi AD (2018) Characterization , preparation , and uses of nanomagnetic Fe_3O_4 impregnated onto fish scale as more efficient adsorbent for Cu^{2+} ion adsorption. Environ Sci Pollut Res 25: 19687. doi.org/10.1007/s11356-018-2058-3

Ahmadpoor F, Shojaosadati SA, Mousavi SZ (2019) PT CR. Int J Biol Macromol (1) 128:941-947. . doi: 10.1016/j.ijbiomac.2019.01.173

Ahmadzadeh S, Desobry S, Keramat J, Nasirpour A (2016) Crystalline structure and morphological properties of porous cellulose/clay composites: The effect of water and ethanol as coagulants. Carbohydr Polym 141:211–219 . doi: 10.1016/j.carbpol.2016.01.017

Awang NA, Wan Salleh WN, Ismail AF, et al (2019) Adsorption Behavior of Chromium(VI) onto Regenerated Cellulose Membrane. Ind Eng Chem Res 58:720–728 . doi: 10.1021/acs.iecr.8b02366

Azlan K, Wansaime WN, Laiken L (2009) Chitosan and chemically modified chitosan beads for acid dyes sorption. Journal of Environmental Sciences 21:296–302 . doi: 10.1016/S1001-0742(08)62267-6

Ballav N, Das R, Giri S, et al (2018) L-cysteine doped polypyrrole (PPy@L-Cyst): A super adsorbent for the rapid removal of Hg^{+2} and efficient catalytic activity of the spent adsorbent for reuse. Chem Eng J 345:621–630 . doi: 10.1016/j.cej.2018.01.093

Ben Arfi R, Karoui S, Mougin K, Ghorbal A (2017) Adsorptive removal of cationic and anionic dyes from aqueous solution by utilizing almond shell as bioadsorbent. Euro-Mediterranean J Environ Integr 2:20. doi: 10.1007/s41207-017-0032-y

Ben Arfi R, Karoui S, Mougin K, Ghorbal A (2019) Cetyltrimethylammonium bromide-treated Phragmites australis powder as novel polymeric adsorbent for hazardous Eriochrome Black T removal from aqueous solutions. Polym Bull 76:5077–5102. doi: 10.1007/s00289-018-2648-8

Bilgin E, Erol K, Köse K, et al (2018) Use of nicotinamide decorated polymeric cryogels as heavy metal sweeper. Environ Sci Pollut Res Int 25(27):27614-27627. doi: 10.1007/s11356-018-2784-6

Bregado JL, Secchi AR, Tavares FW, et al (2019) Amorphous paracrystalline structures from native crystalline cellulose: A molecular dynamics protocol. Fluid Phase Equilibria 491:56–76 . doi: 10.1016/j.fluid.2019.03.011

Chang J, Shen Z, Hu X, et al (2020) Adsorption of Tetracycline by Shrimp Shell Waste from Aqueous Solutions: Adsorption Isotherm, Kinetics Modeling, and Mechanism. ACS Omega 5:3467–3477 . doi: 10.1021/acsomega.9b03781

Chen T, Liu W (2019) Highly Unsaturated Microcrystalline Cellulose and Its Cross-Linked Soybean-Oil-Based Thermoset Composites. ACS Sustain Chem Eng 7:1796–1805 . doi: 10.1021/acssuschemeng.8b05968

631 Dhandole LK, Kim SG, Bae HS, et al (2020) Simultaneous and synergistic effect of
632 heavy metal adsorption on the enhanced photocatalytic performance of a visible-
633 light-driven RS-TONR/TNT composite. Environ Res 180:108651 . doi:
634 10.1016/j.envres.2019.108651

635 Ronda A, Martin-Lara M A, Dioniso E, et al (2013) Effect of lead in biosorption of
636 copper by almond shell. J Taiwan Inst Chem Eng 44:466–473. doi:
637 10.1016/j.jtice.2012.12.019

638 El Rouby WMA, El-Dek SI, Goher ME, Noaemy SG (2018) Efficient water
639 decontamination using layered double hydroxide beads nanocomposites. Environ
640 Sci Pollu Res 70: 1-19. doi: 10.1007/s11356-018-3257-7

641 Fongkaew I, Sehirlioglu A, Limpijumnong S, et al (2017) Core-level binding energy
642 shifts as a tool to study surface processes on $LaAlO_3$ /$SrTiO_3$. J Electron Spec Rel
643 Phenom 218:21–29 . doi: 10.1016/j.elspec.2017.05.009

644 Gao X, Wu L, Xu Q, et al (2018) Adsorption kinetics and mechanisms of copper ions
645 on activated carbons derived from pinewood sawdust by fast H_3PO_4 activation.
646 Environ Sci Pollut Res (2018) 25:7907–7915. https://doi.org/10.1007/s11356-017-
647 1079-7

648 Godiya CB, Cheng X, Li D, et al (2019) Carboxymethyl cellulose/polyacrylamide
649 composite hydrogel for cascaded treatment/reuse of heavy metal ions in
650 wastewater. J Hazard Mater 364:28–38 . doi: 10.1016/j.jhazmat.2018.09.076

651 Hemmati F, Jafari SM, Kashaninejad M, Barani Motlagh M (2018) Synthesis and
652 characterization of cellulose nanocrystals derived from walnut shell agricultural
653 residues. Inter J Biol Macromol 120:1216–1224 . doi:
654 10.1016/j.ijbiomac.2018.09.012

655 Hu Z, Qiu L, Sun Y, et al (2019) Improvement of the solubility and emulsifying
656 properties of rice bran protein by phosphorylation with sodium trimetaphosphate.
657 Food Hydrocolloids 96:288–299 . doi: 10.1016/j.foodhyd.2019.05.037

658 Khan H, Kadam A, Dutt D (2019) Studies on Bacterial Cellulose Produced by a Novel
659 Strain of Lactobacillus Genus. Carbohyd Polym 115513 . doi:
660 10.1016/j.carbpol.2019.115513

661 Lawal IA, Klink M, Ndungu P (2019) Deep eutectic solvent as an efficient modifier of
662 low-cost adsorbent for the removal of pharmaceuticals and dye. Environ Res
663 179:108837 . doi: 10.1016/j.envres.2019.108837

664 Lei H, Pan N, Wang X, Zou H (2018) Facile Synthesis of Phytic Acid Impregnated
665 Polyaniline for Enhanced U(VI) Adsorption. J Chem Eng Data (63)10:3989-3997.
666 doi: 10.1021/acs.jced.8b00688

667 Leone G, Consumi M, Pepi S, et al (2020) Poly-vinyl alcohol (PVA) crosslinked by
668 trisodium trimetaphosphate (STMP) and sodium hexametaphosphate (SHMP):
669 Effect of molecular weight, pH and phosphorylating agent on length of spacing
670 arms, crosslinking density and water interaction. J Molecular Structure
671 1202:127264 . doi: 10.1016/j.molstruc.2019.127264

672 Li X, Li H, You T, et al (2019a) Enhanced Dissolution of Cotton Cellulose in 1-Allyl-3-
673 methylimidazolium Chloride by the Addition of Metal Chlorides. ACS Sustain
674 Chem Eng (7) 23:19176-19184. doi: 10.1021/acssuschemeng.9b05159

675 Li Y, Song S, Xia L, et al (2019b) Enhanced Pb(II) removal by algal-based biosorbent
676 cultivated in high-phosphorus cultures. Chem Eng J 361:167–179 . doi:
677 10.1016/j.cej.2018.12.070

678 Liu K, Cheng X, Ma Y, et al (2019) Analysis of interfacial nanostructure and interaction
679 mechanisms between cellulose fibres and calcium silicate hydrates using
680 experimental and molecular dynamics simulation data. Appl Surf Sci 506: 144914 .
681 doi: 10.1016/j.apsusc.2019.144914

682 Liu P, Borrell PF, Božič M, et al (2015) Nanocelluloses and their phosphorylated
683 derivatives for selective adsorption of Ag^{+}, Cu^{2+} and Fe^{3+} from industrial effluents.
684 J Hazard Mater 294:177–185 . doi: 10.1016/j.jhazmat.2015.04.001

685 Lü T, Qi D, Zhang D, et al (2019) One-step synthesis of versatile magnetic
686 nanoparticles for efficiently removing emulsified oil droplets and cationic and
687 anionic heavy metal ions from the aqueous environment. Environ Sci Pollut Res
688 Int 26(6):6153-6166. doi: 10.1007/s11356-018-4002-y.

689 Luo H, Zeng X, Liao P, et al (2019) Phosphorus removal and recovery from water with
690 macroporous bead adsorbent constituted of alginate-Zr^{4+} and PNIPAM-
691 interpenetrated networks. Inter J Biol Macromol 199:170-177 . doi:
692 10.1016/j.ijbiomac.2018.12.269

693 Luo P, Liu L, Xu W, et al (2018a) Preparation and characterization of aminated
694 hyaluronic acid/oxidized hydroxyethyl cellulose hydrogel. Carbohydr Polym
695 199:170–177 . doi: 10.1016/j.carbpol.2018.06.065

696 Luo W, Bai Z, Zhu Y (2018b) Fast removal of Co(II) from aqueous solution using
697 porous carboxymethyl chitosan beads and its adsorption mechanism. RSC
698 Advances 8:13370–13387 . doi: 10.1039/c7ra13064c

699 Ma X, Liu C, Anderson DP, Chang PR (2016) Porous cellulose spheres : Preparation ,
700 modi fi cation and adsorption properties. Chemosphere 165:399–408 . doi:
701 10.1016/j.chemosphere.2016.09.033

702 Maaloul N, Oulego P, Rendueles M, et al (2017a) Novel biosorbents from almond
703 shells : Characterization and adsorption properties modeling for Cu (II) ions from
704 aqueous solutions. J Environ Chem Eng (5)3: 2944-2954. doi:
705 10.1016/j.jece.2017.05.037

706 Maaloul N, Arfi R Ben, Rendueles M, et al (2017b) Dialysis-free extraction and
707 characterization of cellulose crystals from almond (Prunus dulcis) shells. J Mater
708 Environ Sci 8(11):4171–4181.
709 https://www.jmaterenvironsci.com/Document/vol8/vol8_N11/438-JMES-2556-
710 Maaloul

711 Maaloul N, Oulego P, Rendueles M (2019) Synthesis and characterization of eco-
712 friendly cellulose beads for copper (II) removal from aqueous solutions. Environ
713 Sci Pollut Res 1-17. doi.org/10.1007/s11356-018-3812-2.

714 Maniscalco MP, Corrado C, Volpe R, Messineo A (2020) Evaluation of the optimal
715 activation parameters for almond shell bio-char production for capacitive
716 deionization. Bioresour Technol Reports 11:100435 . doi:
717 10.1016/j.biteb.2020.100435

718 Mikoda B (2018) Air pollution control and flue gas desulfurization residues from Polish
719 copper smelting facility as adsorbents of Pb (II) and Cu (II) from aqueous
720 solutions. Environ Sci Pollut Res 25(31): 31520–31534. doi: 10.1007/s11356-018-
721 3133-5

722 Milani PA, Debs KB, Labuto G, Carrilho ENVM (2018) Agricultural solid waste for
723 sorption of metal ions: part I—characterization and use of lettuce roots and
724 sugarcane bagasse for Cu(II), Fe(II), Zn(II), and Mn(II) sorption from aqueous
725 medium. Environ Sci Pollut Res 25(36):35895-35905. doi: 10.1007/s11356-018-
726 1615-0

727 Neris JB, Luzardo FHM, da Silva EGP, Velasco FG (2018) Evaluation of adsorption
728 processes of metal ions in multi-element aqueous systems by lignocellulosic
729 adsorbents applying different isotherms: A critical review. Chem Eng J 357: 404-
730 420. doi: 10.1016/j.cej.2018.09.125

731 Oh W-D, Lee MG-H, Chanaka Udayanga WD, et al (2019) Insights into the single and
732 binary adsorption of copper(II) and nickel(II) on hexagonal boron nitride:
733 Performance and mechanistic studies. J Environ Chem Eng 7:102872 . doi:
734 10.1016/j.jece.2018.102872

735 Olivera S, Venkatesh K, Reddy N, et al (2018) Oxygen enriched network-type carbon
736 spheres for multipurpose water purification applications. Environm Technol Innov
737 12:160–171 . doi: 10.1016/j.eti.2018.08.007

738 Orliukas AF, Venckutė V, Miskinis J, et al (2013) X-ray Photoelectron and Broadband
739 Impedance Spectroscopy of $Li_{1+4x}Ti_{2-x}(PO_4)_3$ Solid Electrolyte Ceramics.
740 Lithuanian J Phys 5332:244–254 . doi: 10.1149/2.072207jes

741 Othmani A, Kesraoui A, Seffen M (2017) The alternating and direct current effect on
742 the elimination of cationic and anionic dye from aqueous solutions by
743 electrocoagulation and coagulation flocculation. Euro-Mediterranean J Environ
744 Integr 2:6. doi: 10.1007/s41207-017-0016-y

745 Oun AA, Rhim J-W (2019) Preparation of multifunctional carboxymethyl cellulose-
746 based films incorporated with chitin nanocrystal and grapefruit seed extract. Inter J
747 Biol Macromol. doi: 10.1016/j.ijbiomac.2019.10.191

748 Putra RN, Lee YH (2019) Separation and Puri fi cation Technology Entrapment of
749 micro-sized zeolites in porous hydrogels : Strategy to overcome drawbacks of
750 zeolite particles and beads for adsorption of ammonium ions. Sep Purif Technol
751 116351 . doi: 10.1016/j.seppur.2019.116351

752 Qi X, Liu R, Chen M, et al (2019) Removal of copper ions from water using
753 polysaccharide-constructed hydrogels. Carbohydr Polym 209:101-110.
754 doi.org/10.1016/j.carbpol.2019.01.015

755 Qi X, Wu L, Su T, et al (2018) Polysaccharide-based cationic hydrogels for dye

adsorption. Colloids Surf B: Biointerf 170:364–372 . doi: 10.1016/j.colsurfb.2018.06.036

Ram B, Chauhan GS (2018) New spherical nanocellulose and thiol-based adsorbent for rapid and selective removal of mercuric ions. Chem Eng J 331:587–596 . doi: 10.1016/j.cej.2017.08.128

Reid MS, Villalobos M, Cranston ED (2017) The role of hydrogen bonding in non-ionic polymer adsorption to cellulose nanocrystals and silica colloids. Curr Opin Colloid Interf Sci 29:76–82 . doi: 10.1016/j.cocis.2017.03.005

Rol F, Sillard C, Bardet M, et al (2020) Cellulose phosphorylation comparison and analysis of phosphorate position on cellulose fibers. Carbohydr Polym 229:115294 . doi: 10.1016/j.carbpol.2019.115294

Sánchez-Reséndiz A, Rodríguez-Barrientos S, Rodríguez-Rodríguez J, et al (2018) Phosphoesterification of soybean and peanut proteins with sodium trimetaphosphate (STMP): Changes in structure to improve functionality for food applications. Food Chemistry 260:299–305 . doi: 10.1016/j.foodchem.2018.04.009

Singh DK, Kumar V, Mohan S, Hasan SH (2017) Polylysine Functionalized Graphene Aerogel for the Enhanced Removal of Cr(VI) through Adsorption: Kinetic, Isotherm, and Thermodynamic Modeling of the Process. J Chem Eng Data 62:1732–1742 . doi: 10.1021/acs.jced.7b00188

Somsesta N, Sricharoenchaikul V, Aht-Ong D (2020) Adsorption removal of methylene blue onto activated carbon/cellulose biocomposite films: Equilibrium and kinetic studies. Mater Chem Phys 240:122221 . doi: 10.1016/j.matchemphys.2019.122221

Souto-maior FA, Reis V, Pedreiro L N et al (2010) Phosphated crosslinked pectin as a potential excipient for specific drug delivery : preparation and physicochemical characterization. Polym Intern 127–135 . doi: 10.1002/pi.2700

Stanciu MC, Nichifor M (2018) Influence of dextran hydrogel characteristics on adsorption capacity for anionic dyes. Carbohydr Polym 199:75–83 . doi: 10.1016/j.carbpol.2018.07.011

Syafiuddin A, Salmiati S, Jonbi J, Fulazzaky MA (2018) Application of the kinetic and isotherm models for better understanding of the behaviors of silver nanoparticles adsorption onto different adsorbents. J Environ Managtt 218:59–70 . doi: 10.1016/j.jenvman.2018.03.066

Tao Y, Zhang R, Xu W, et al (2016) Rheological behavior and microstructure of release-controlled hydrogels based on xanthan gum crosslinked with sodium trimetaphosphate. Food Hydrocolloids 52:923–933 . doi: 10.1016/j.foodhyd.2015.09.006

Wang K, Tian Z, Yin N (2018a) Significantly Enhancing Cu(II) Adsorption onto Zr-MOFs through Novel Cross-Flow Disturbance of Ceramic Membrane. Ind Eng Chem Res 57:3773–3780 . doi: 10.1021/acs.iecr.7b04850

Wang N, Feng Z, Ma X, Zheng P (2017) The modification of rectorite with carbon layers and trisodium trimetaphosphate for the removal of Pb^{2+}. Applied Clay Science 146:115–121 . doi: 10.1016/j.clay.2017.05.044

798 Wang P, Tang Y, Liu Y, et al (2018b) Halloysite nanotube@carbon with rich carboxyl
799 groups as a multifunctional adsorbent for the efficient removal of cationic Pb(II),
800 anionic Cr(VI) and methylene blue (MB). Environ Sci: Nano 5:2257-2268. doi:
801 10.1039/C8EN00561C

802 Wang W, Zhang H, Shen J, Ye M (2018c) Facile preparation of magnetic chitosan/poly
803 (vinyl alcohol) hydrogel beads with excellent adsorption ability via freezing-
804 thawing method. Colloids Surf A: Physicochem Eng Aspects 553:672-680.
805 doi.org/10.1016/j.colsurfa.2018.05.094

806 Wang X, Jing S, Hou Z, et al (2018d) Permeable, robust and magnetic hydrogel beads:
807 water droplet templating synthesis and utilization for heavy metal ions removal. J
808 Mater Sci 53:15009–15024 . doi: 10.1007/s10853-018-2681-x

809 Weber W J, Morris J C (1963) Kinetics of Adsorption of Carbon from Solution. J San En
810 Div 89 (1), 31-60.

811 Wen Z, Huang K, Niu Y, et al (2020) Kinetic study of ultrasonic-assisted uranium
812 adsorption by anion exchange resin. Colloids Surf A: Physicochem Eng Aspects
813 585:124021 . doi: 10.1016/j.colsurfa.2019.124021

814 Xie Y, Zhang B, Li MN, Chen HQ (2019) Effects of cross-linking with sodium
815 trimetaphosphate on structural and adsorptive properties of porous wheat starches.
816 Food Chem 289:187–194 . doi: 10.1016/j.foodchem.2019.03.023

817 Yang K, Fox J (2018) DPF soot as an adsorbent for Cu(II), Cd(II), and Cr(VI)
818 compared with commercial activated carbon. Environ Sci Pollut Res 25:8620–
819 8635 . doi: 10.1007/s11356-017-1122-8

820 Yang X, Dong Z, Zhang M, et al (2020) Selective Recovery of Ag(I) Using a Cellulose-
821 Based Adsorbent in High Saline Solution. J Chem Eng Data. doi:
822 10.1021/acs.jced.9b01107

823 Zhan W, Gao L, Fu X, et al (2019) Green synthesis of amino-functionalized carbon
824 nanotube-graphene hybrid aerogels for high performance heavy metal ions
825 removal. Applied Surf Sci 467-468:1122–1133 . doi:
826 10.1016/j.apsusc.2018.10.248

827 Zhang X, Lin X, He Y, et al (2019) Study on adsorption of tetracycline by Cu-
828 immobilized alginate adsorbent from water environment. Inter J Biol Macromol
829 124:418–428. 10.1016/j.ijbiomac.2018.11.218

830 Zhang X, Yan L, Li J, Yu H (2020) Adsorption of heavy metals by L-cysteine
831 intercalated layered double hydroxide: Kinetic, isothermal and mechanistic studies.
832 J Colloid Interf Sci 562:149–158 . doi: 10.1016/j.jcis.2019.12.028

833 Zhou J, He Y, Chen Y, et al (2018) Adsorption of phosphorus from slaughterhouse
834 wastewater by carboxymethyl konjac glucomannan loaded with lanthanum. Inter J
835 Biol Macromol 119:105–115 . doi: 10.1016/j.ijbiomac.2018.07.140

836 Zhuang X, Zhan H, Song Y, et al (2019) Insights into the evolution of chemical
837 structures in lignocellulose and non-lignocellulose biowastes during hydrothermal
838 carbonization (HTC). Fuel 236:960–974 . doi: 10.1016/j.fuel.2018.09.019

Figures

Figure 1

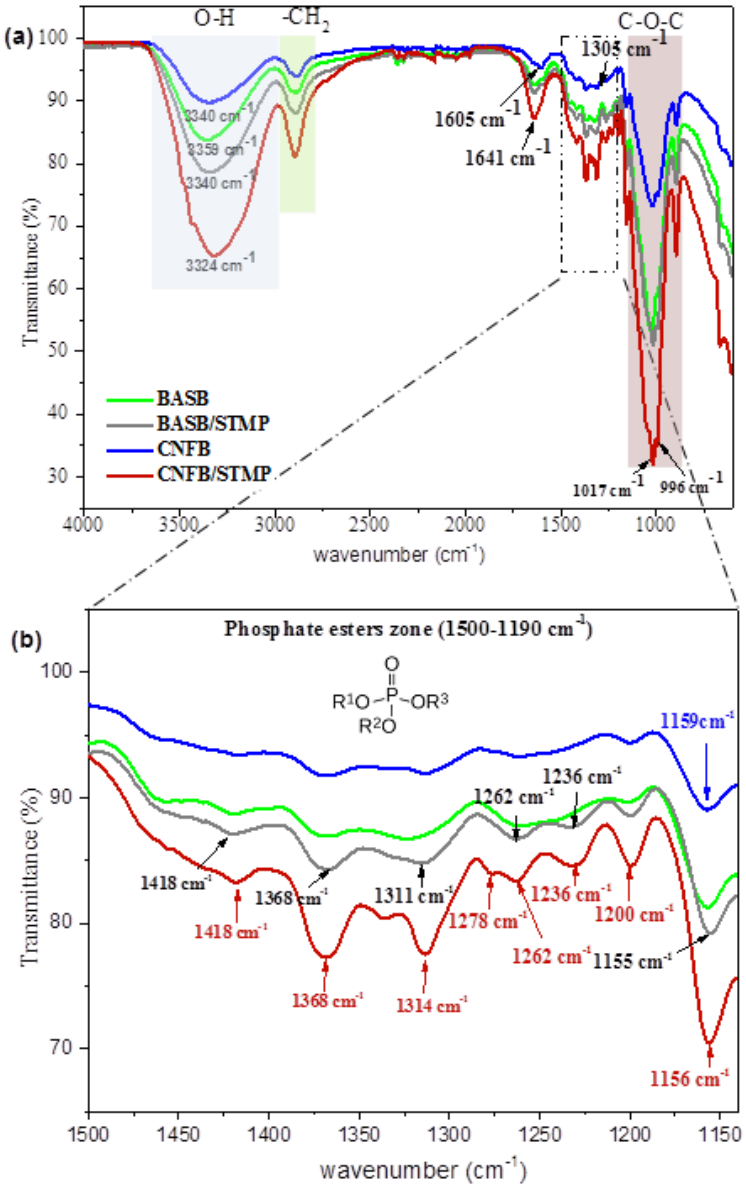

Fig. 1 FTIR spectra of BASB, BASB/STMP, CNFB and CNFB/STMP adsorbents: **(a)** at 4000–600 cm^{-1}; **(b)** magnified spectra in the range 1500–1190 cm^{-1}

Figure 2

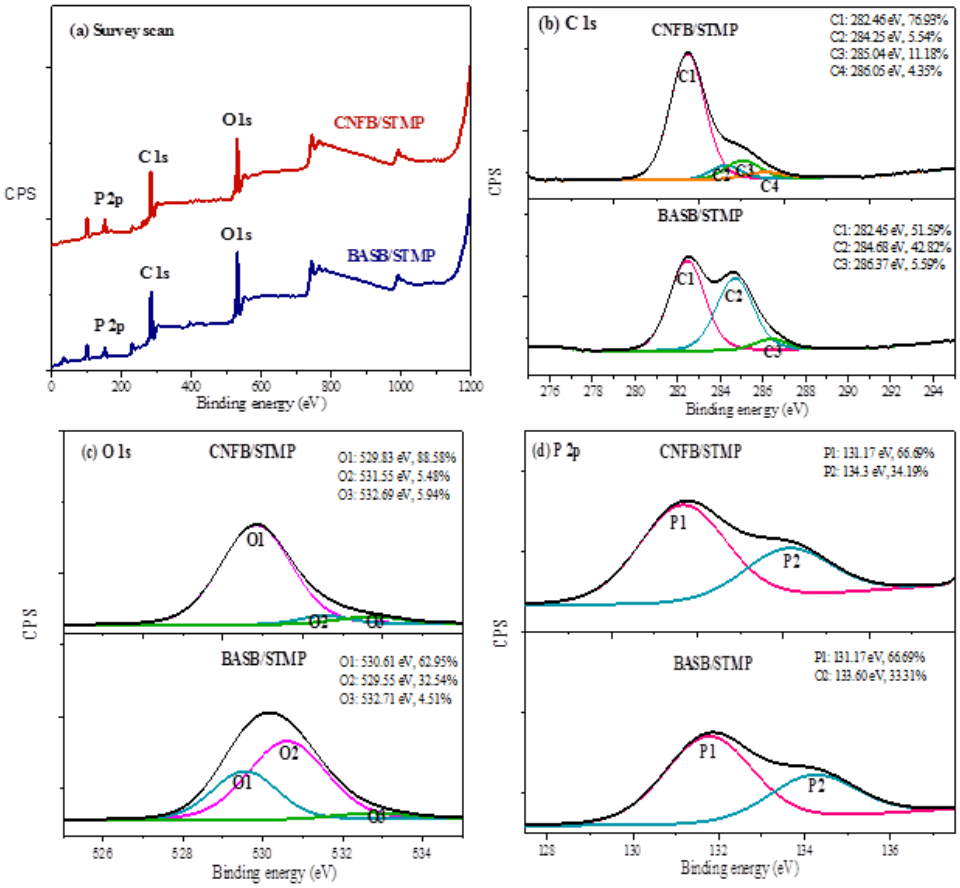

Fig. 2 (a) XPS survey scan and b) high resolution spectra of C1s, **(c)** O1s, **(d)** P2p orbitals of BASB/STMP and CNFB/STMP samples

Figure 3

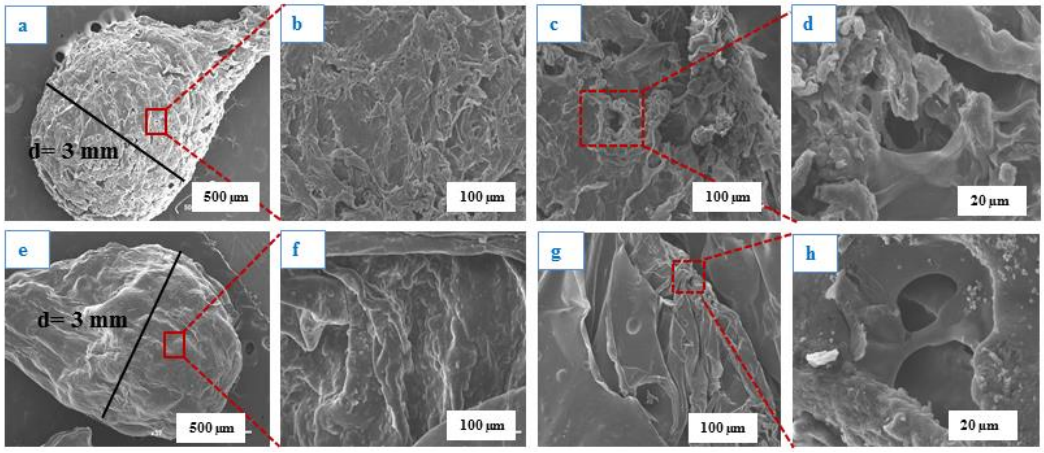

Fig. 3 SEM images at different magnifications of the STMP-functionalized beads: **(a-d)** BASB/STMP and **(e-h)** CNFB/STMP

849 **Figure 4**

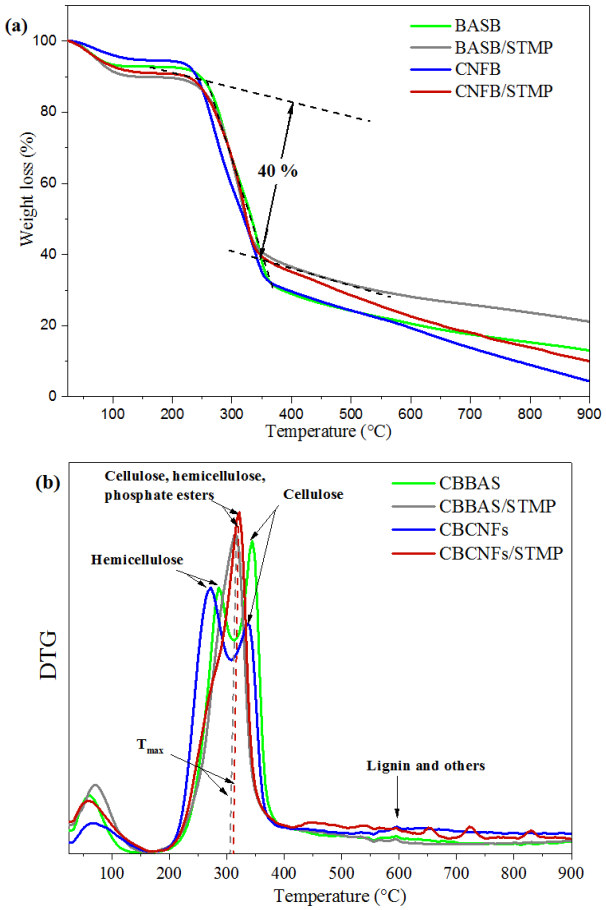

850 **Fig. 4** Thermogravimetric analysis of BASB, CNFB, BASB/STMP and CNFB/STMP
851 adsorbents: **(a)** TGA and **(b)** DTG curves

852 **Figure 5**

853

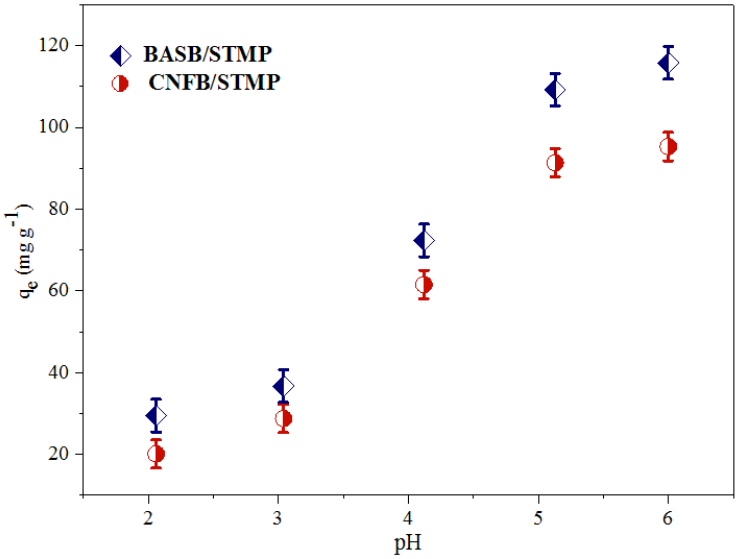

854 **Fig. 5** Effect of pH on the adsorption capacity of Cu(II) ions from aqueous solution by
855 BASB/STMP and CNFB/STMP adsorbents. In all cases: temperature: 30 °C, contact
856 time: 2 h, adsorbent dosage: 0.5 g L^{-1} and initial concentration of pollutant: 200 mg L^{-1}

Figure 6

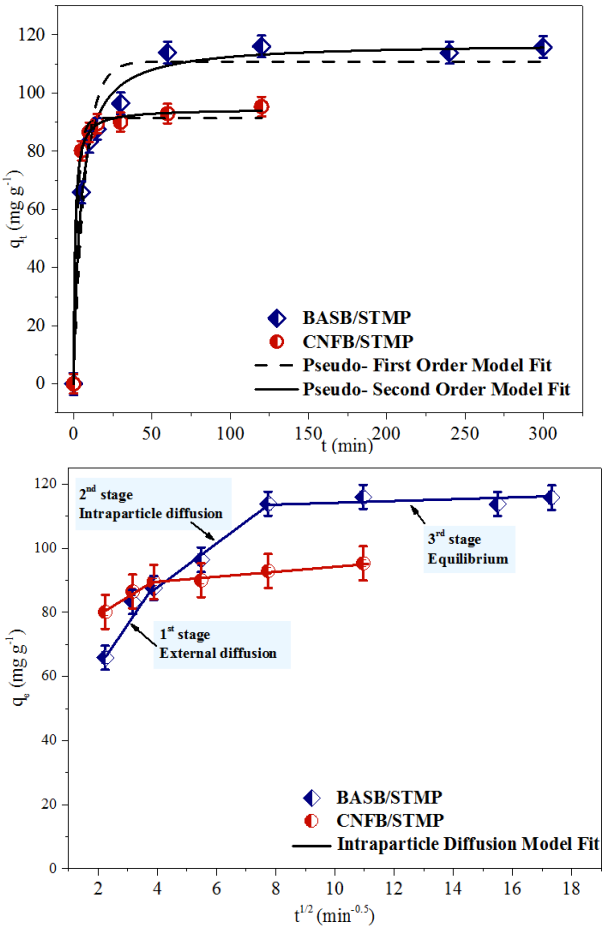

Fig. 6 Time-dependent adsorption curves of Cu(II) ion adsorption on BASB/STMP and CNFB/STMP and the non-linear fitting plots of kinetic data for **(a)** pseudo-first order and pseudo-second order models, and **(b)** intraparticle diffusion model

Figure 7

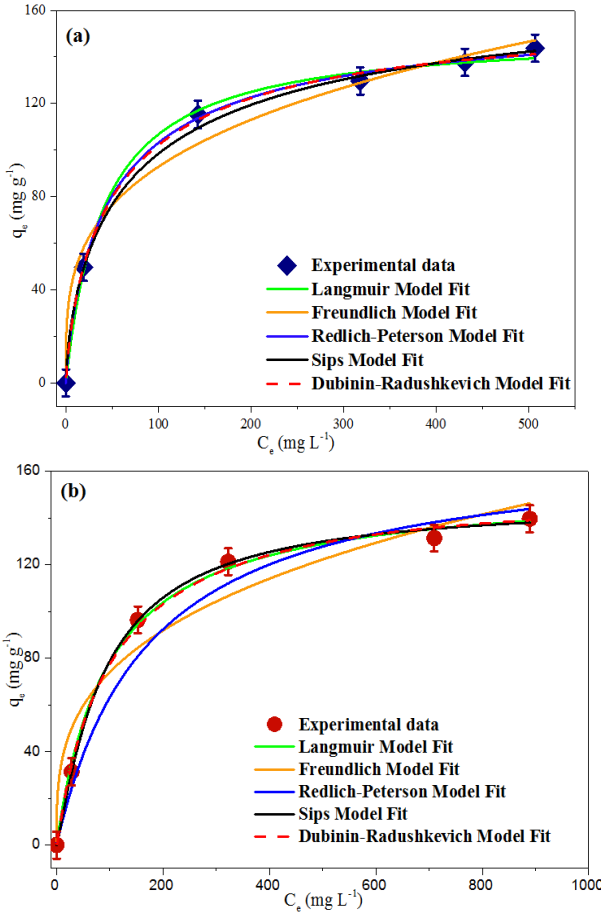

Fig. 7 Adsorption isotherms of Cu(II) at 30 °C and the corresponding fitting plots for Langmuir, Freundlich, Redlich-Peterson, Sips and Dubinin-Radushkevich models **(a)** BASB/STMP and **(b)** CNFB/STMP

865 **Figure 8**

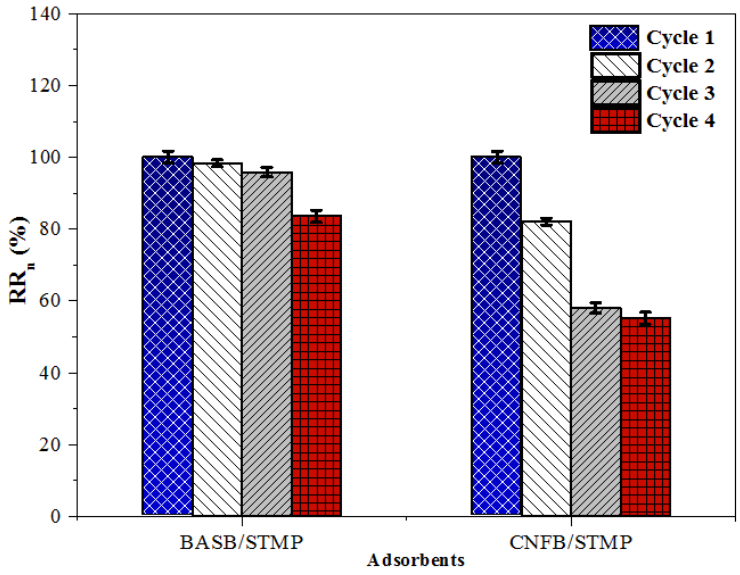

866 **Fig. 8** Regeneration rate of BASB/STMP and CNFB/STMP adsorbents for four recycles

867 **Figure 9**

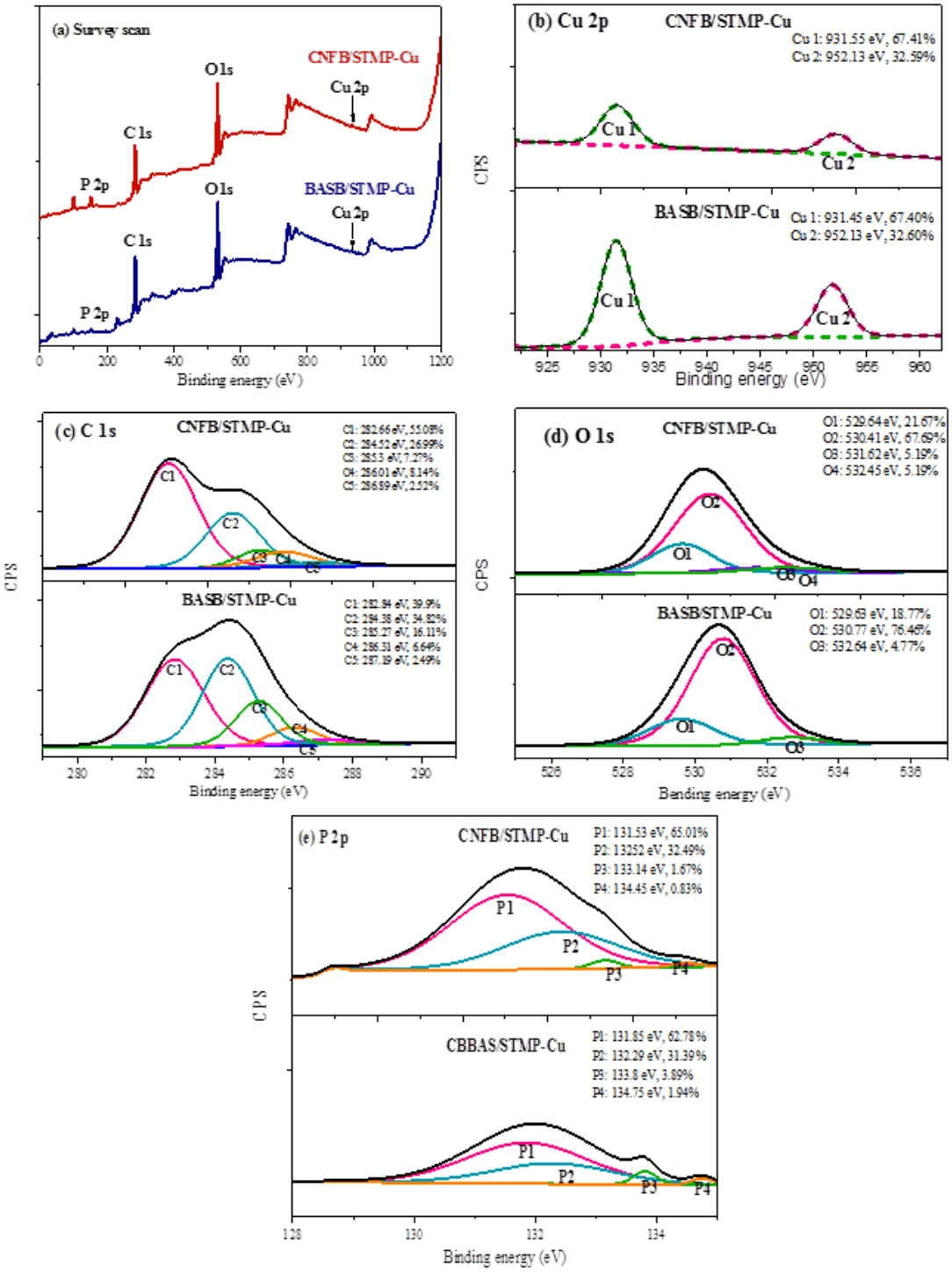

868

869 **Fig. 9 (a)** XPS survey scan spectra and high resolution scan spectra of **(b)** Cu2p, **(c)**
870 C1s, **(d)** O1s and **(e)** P2p for BASB/STMP and CNFB/STMP after copper adsorption

871

872

873 # Tables

874 **Table 1** Comparison of the BET specific surface area of various adsorbents

Sample	Specific surface area ($m^2 g^{-1}$)	References
Almond shell	0.406	(Ronda et al. 2013)
Bleached almond shell (BAS)	0.51	(Maaloul et al. 2017a)
Lyophilized- bleached almond shell (L-BAS)	0.99	
TEMPO oxidized cellulose nanofibers for 1 h (TOCN1)	1.66	
TEMPO oxidized cellulose nanofibers for 2 h (TOCN2)	1.97	
Chitosan beads	0.96	(Azlan et al. 2009)
Chitosan-EGDE beads	0.62	
Carbon spheres (CSs)	1.02	(Olivera et al. 2018)
Chitosan-coated filter with skewed hexagonal holes	0.254	(Zhang et al. 2019a)
Chitosan-coated filter with skewed round holes	0.183	
Chitosan-coated filter with square-shaped holes	0.205	
Chitosan-coated filter with hexagonal-shaped holes	0.254	
CMC beads	0.49	(Luo et al. 2018b)
BASB	0.007	Present work
BASB/STMP	0.87	Present work
CNFB	0.57	Present work
CNFB/STMP	1.22	Present work

875 **Table 2** Kinetic parameters for the adsorption of Cu(II) ions onto BASB/STMP and
876 CNFB/STMP adsorbents

Models	**Parameters**	**BASB/STMP**	**CNFB/STMP**
Experimental data	$q_{e,exp}$ (mg g^{-1})	116.25	93.65
Pseudo-first order	$q_{e,cal,}$ (mg g^{-1})	110.76	91.38
	k_1 (min^{-1})	0.141	0.402
	R^2	0.956	0.994
	χ^2	60.944	0.609
Pseudo-second order	$q_{e,cal}$ (mg g^{-1})	117.21	94.54
	k_2 (mg $g^{-1}min^{-1}$)	0.002	0.011
	R^2	0.991	0.998
	χ^2	12.770	0.098
Intraparticle diffusion	$k_{id,1}$ (mg g^{-1} $min^{-0.5}$)	13.554	5.748
	$k_{id,2}$ (mg g^{-1} $min^{-0.5}$)	6.851	0.876
	$k_{id,3}$ (mg g^{-1} $min^{-0.5}$)	0.073	
	I_1 (mg g^{-1})	36.990	67.602
	I_2 (mg g^{-1})	60.265	85.766
	I_3 (mg g^{-1})	113.925	
	$(R_1)^2$	0.871	0.963
	$(R_2)^2$	0.984	0.963
	$(R_3)^2$	0.390	

877 **Table 3** Isotherms parameters for the adsorption of Cu(II) ions onto STMP modified
878 beads

Isotherms	**Parameters**	**BASB/STMP**	**CNFB/STMP**
Experimental data		143.74	139.59
Langmuir	q_{max} (mg g^{-1})	150.73	153.59
	K_L (L mg^{-1})	0.024	0.010
	R_L	0.056	0.094
	R^2	0.997	0.997
	χ^2	9.666	10.778
Freundlich	q_{cal} (mg g^{-1})	101.79	146.21
	K_F (mg g^{-1})(L $mg^{-1})^{1/n_F}$	25.142	17.608
	n_F	3.525	3.208
	R^2	0.981	0.942
	χ^2	63.029	193.371
Sips	q_{max} (mg g^{-1})	180.46	147.90
	k_S (L mg^{-1})	0.013	0.011
	n_S	1.421	0.872
	R^2	0.988	0.999
	χ^2	9.187	0.472
Redlich-Peterson	q_{max} (mg g^{-1})	141.44	143.79
	K_{R-P} (L g^{-1})	4.437	1
	a_{R-P} (L $mg^{-1})^{B_{R-P}}$	0.045	0.006
	B_{R-P}	0.931	1
	R^2	0.998	0.956
	χ^2	0.168	147.437
Dubinin-Radushkevich	q_{D-R} (mg g^{-1})	153.59	148.20
	K_{D-R} (mol^2 kJ^{-2})	0.003	0.006
	E (kJ mol^{-1})	12.91	9.13
	R^2	0.998	0.996
	χ^2	0.185	0.361

879

880

881 **Table 4** Comparison of the maximum sorption capacities of Cu(II) by different

882 adsorbents in the literature

Adsorbents	Adsorbents type	q_{max}[a] (mg g^{-1})	Time	pH	Isotherm	Order of reaction	References
Pinewood sawdust activated carbon with H_3PO_4 (IR1-500)	Particle	20.2	60 min	6.0	-	PSO	(Gao et al. 2018)
Pinewood sawdust activated carbon with H_3PO_4 (IR4-800)	Particle	11.5	60 min	6.0	-	PSO	
Zr-based metal-organic frameworks (Zr-MOFs)	MOFs	59.8	12 h	6.0	-	PSO	(Wang et al. 2018a)
PEI-coated Fe_3O_4	Nanoparticle	66.6	10 min	5.0	Langmuir	PSO	(Lü et al. 2019)
Fish scale (FS)	Powder	61.73	150 min	6.0	Langmuir		(Ahmadifar and Koohi 2018)
Nanomagnetic (Fe_3O_4) loaded fish scale (MFS)	Powder	103.1	120 min	6.0	Langmuir		
LDH-chitosan-alginate beads	Bead	24.75	2 h	5.0	Freundlich	PSO	(El Rouby et al. 2018)
CNFs functionalized with phosphate and carboxylic groups	Powder	114	12 h	7.0	-	-	(Liu et al. 2015)
Magnetic silica coated iron carbide/alginate beads	Bead	37.73	60 min	3-4	Sips	PSO	(Ahmadpoor et al. 2019)
Porous cellulose sphere	Bead	110.7	60 min	7.0	Langmuir	PSO	(Du et al. 2018)
Thiosemicarbazide modified green carboxymethyl cellulose	Powder	144.9	30 min	6.0	Langmuir	PSO	(Ahmad et al. 2018)
Bleached almond shell (BAS)	Powder	18.71	45 min	6.04	Temkin	PFO	(Maaloul et al. 2017a)
Lyophilized bleached almond shell (L-BAS)	Powder	28.27	45 min	6.04	Langmuir	PSO	
TEMPO oxidized cellulose nanofibers for 1 h (TOCN1)	Powder	23.8	45 min	6.04	Langmuir	PSO	
TEMPO oxidized cellulose nanofibers for 2 h (TOCN2)	Powder	21.57	45 min	6.04	Langmuir	PSO	
CBBAS	Bead	128.24	2 h	6.0	Sips	PSO	(Maaloul et al. 2019)
BASB/STMP	Bead	141.44	2 h	6.0	Redlich-Peterson	PSO	Present work
CNFB/STMP	Bead	147.90	2 h	6.0	Sips	PSO	Present work

883 **q_{max}[a]**: maximum adsorption capacity of copper (mg g^{-1}); **PFO**: Pseudo-first order kinetic model; **PSO**:

884 Pseudo-second order kinetic model.

885

886

887

888

889

890

891

892

893

894

895

Supplementary Material to

'Enhanced Cu(II) adsorption using sodium trimetaphosphate modified cellulose beads: equilibrium, kinetics, adsorption mechanisms and reusability'

Najeh Maaloul[1], Paula Oulego[2], Manuel Rendueles[2], Achraf Ghorbal[1,3], Mario Díaz[2*]

[1]Applied Thermodynamic Research Laboratory LR18ES33, National Engineering School of Gabes, University of Gabes, Avenue Omar Ibn El Khattab 6029 Gabes, Tunisia.

[2] Department of Chemical and Environmental Engineering, University of Oviedo, C/ Julián Clavería s/n, E-33071 Oviedo, Spain.

[3] Higher Institute of Applied Sciences and Technology of Gabes, University of Gabes, Avenue Omar Ibn El Khattab 6029 Gabes, Tunisia.

(5 Pages, 3 Figures)

Table of contents

*Corresponding author's e-mail: mariodiaz@uniovi.es

1. N_2 adsorption – desorption isotherms of BASB, BASB/STMP, CNFB and CNFB/STMP adsorbents (Fig. S1)

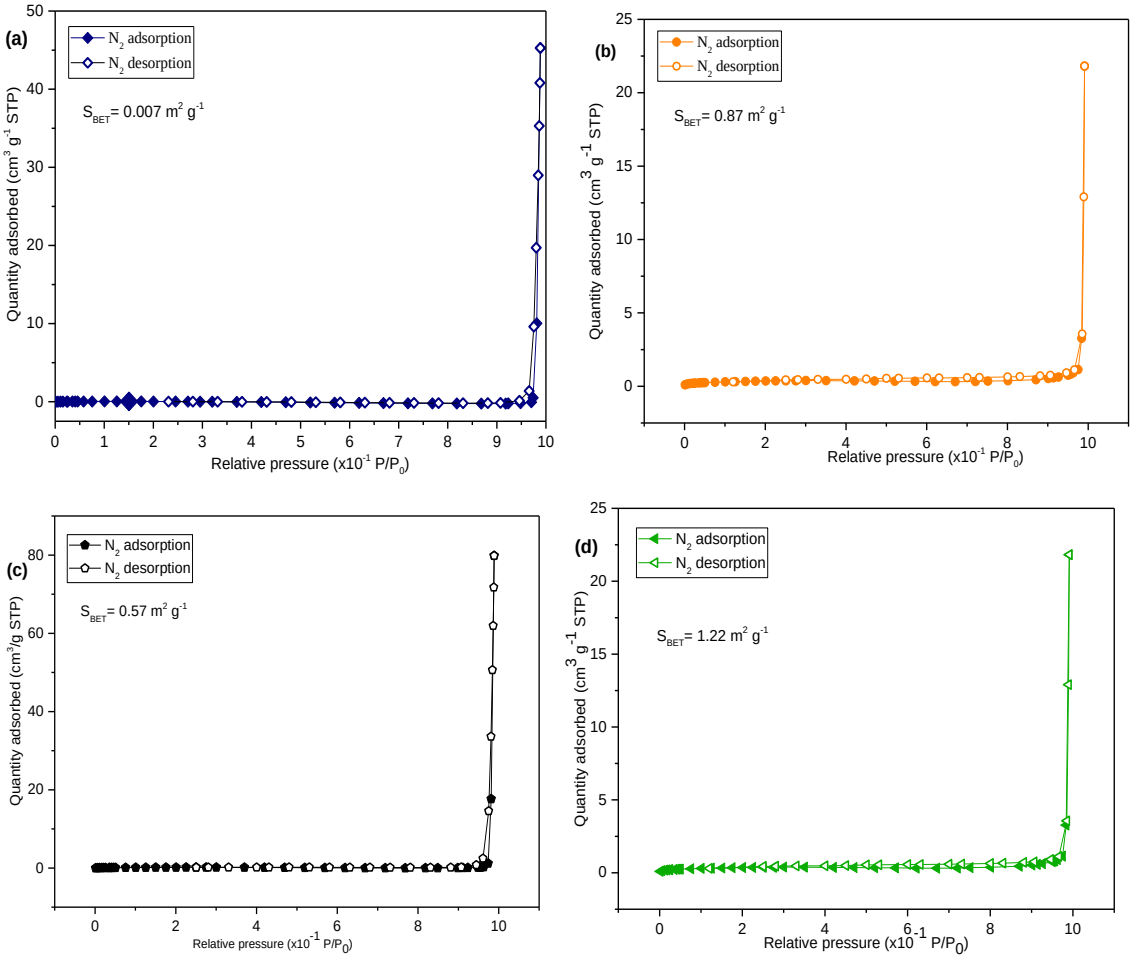

Fig. S1 N_2 adsorption – desorption isotherms of **(a)** BASB, **(b)** BASB/STMP, **(c)** CNFB and **(d)** CNFB/STMP adsorbents

2. Swelling behavior of BASB, BASB/STMP, CNFB and CNFB/STMP adsorbents (Fig. S2)

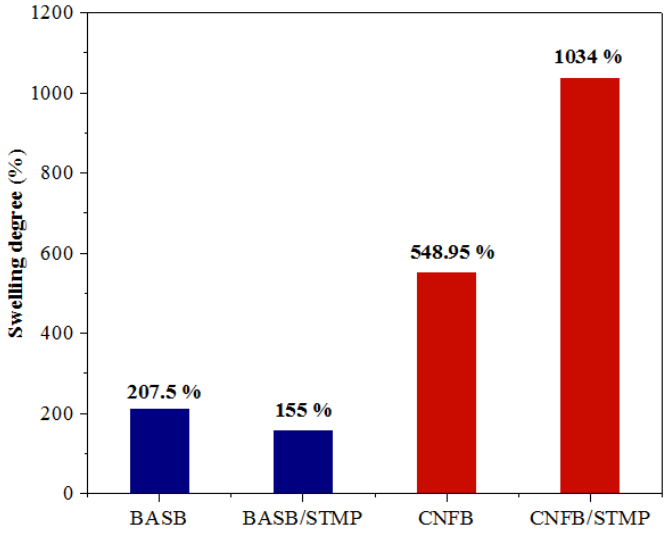

Fig. S2 Swelling properties of the BASB, BASB/STMP, CNFB and CNFB/STMP adsorbents.

3. Determination of the pH_{PZC} of BASB/STMP and CNFB/STMP adsorbents (Fig. S3).

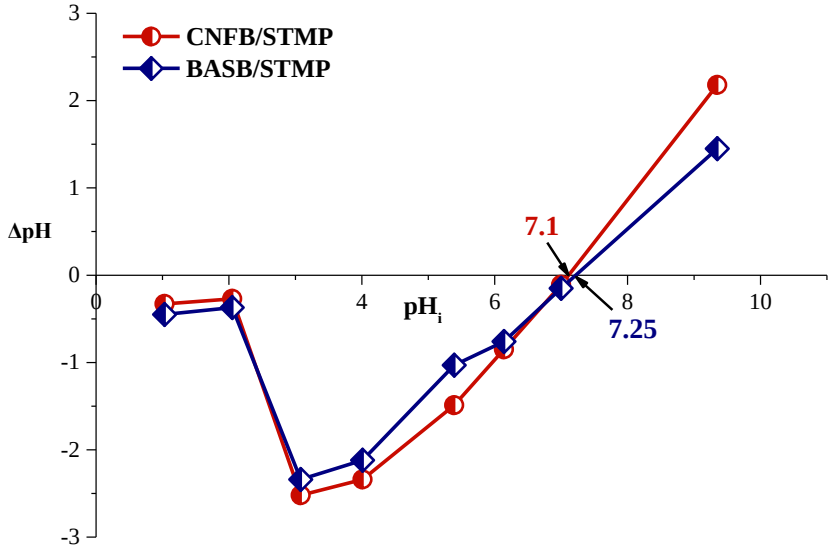

Fig. S3 Determination of the pH_{PZC} value of BASB/STMP and CNFB/STMP adsorbents

4. Isotherm models

The Langmuir Eq. (8), Freundlich Eq. (9) and Sips Eq. (11) isotherm models were fitted to the experiment data using the following equation:

$$q_e = \frac{q_{\max} K_L C_e}{1 + K_L C_e} \tag{8}$$

where q_e is the equilibrium adsorption capacity (mg g^{-1}), q_{max} is the maximum adsorption capacity (mg g^{-1}), C_e is the equilibrium concentration (mg L^{-1}), and K_L is Langmuir constant (L mg^{-1}).

$$q_e = K_F C_e^{1/n_F} \tag{9}$$

where K_F represents Freundlich constant, which can be used to measure the adsorption capacity ((mg g^{-1})(L $mg^{-1})^{1/n_F}$)) and n_F represents the represents the heterogeneity factor.

$$q_e = \frac{q_{max} (C_e k_S)^{1/n_S}}{(1 + C_e k_S)^{1/n_S}} \tag{11}$$

In which k_S is the Sips isotherm constant (L mg^{-1}) and n_S is the Sips model exponent.

Redlich–Peterson Eq. (11) and Dubinin-Raduskevich Eq. (12) (Dubinin, 1960) were also used to analyze the adsorption behavior, their respective equations being as follows:

$$q_e = \frac{K_{R-P} C_e}{1 + a_{R-P} C_e^{B_{R-P}}} \tag{10}$$

where B_{R-P} is the Redlich–Peterson exponent that lies between 0 and 1, K_{R-P} (L g^{-1}) and a_{R-P} (L $mg^{-1})^{B_{R-P}}$ are the Redlich-Peterson constants.

$$q_e = q_{D-R} e^{-K_{D-R} \varepsilon^2} \tag{12}$$

where K_{D-R} is the Dubinin-Radushkevich constant related to the sorption energy (mol^2 kJ^{-2}), q_{D-R} is the adsorption capacity in the D-R model (mg g^{-1}) and ε (kJ mol^{-1}) is the D−R adsorption potential energy obtained through Eq. (13).

$$\varepsilon = RT \ln\left(1 + \frac{1}{C_e}\right) \tag{13}$$

The mean free energy (E, kJ mol^{-1}) of adsorption for each molecule of adsorbate is calculated as per equation (14).

$$E = \frac{1}{\sqrt{2K_{D-R}}} \quad (14)$$

R and T are the universal gas constant (8.314 J mol^{-1} K^{-1}) and the absolute temperature (K), respectively.

References

Dubinin M M (1960) The potential theory of adsorption of gases and vapors for adsorbents with energetically non-uniform surface. Chem Rev 60:235–266. doi/10.1021/cr60204a006